Biomaterials
Science

PAPER

View Article Online
View Journal

Cite this: DOI: 10.1039/d6bm00417b

A multifunctional chemotactic-antibacterial ChMA–AgNPs hydrogel for the treatment of carbapenem-resistant *Pseudomonas aeruginosa*-infected wounds

Xinxin Su,†[a,b] Morui Gui,†[a] Tingna Luo,[b] Qiqi Liu,[b] Xiaohong Zhao,[b] Yicheng Guo,[b] Rixing Zhan,[b] Zhongshuo Hao,[a] Xisheng Xu,*[c] Shuncai Liu*[a] and Zhenyu Gong *[a]

Carbapenem-resistant *Pseudomonas aeruginosa* (CRPA) wound infections are very pathogenic and highly resistant to some other drugs. Passive antimicrobial dressings are conventional, but lack effectiveness, which is a problem in the management of wounds. The objective of this research study is to elucidate the chemotactic effects of L-lysine on the clinically relevant *CRPA* and construct a multifunctional hydrogel dressing that integrates the task of active chemotaxis and antimicrobial effects. Initially, *in vitro* chemotaxis assays, such as agar assays, were used to confirm the potent and specific chemotactic activity of L-lysine against *CRPA*. The bacteria exhibited a tendril-like movement that corresponds to positively charged mediators. Then, a ChMA–AgNPs composite hydrogel was prepared based on a methacrylamide chitosan (ChMA) with L-lysine and silver nanoparticles (AgNPs) loaded on it. Physicochemical characterization indicated that the AgNPs were firmly encased in the material without being leached substantially, thereby minimizing tissue toxicity by silver ions. The concentration gradient of L-lysine directed bacteria towards the hydrogel, facilitating the targeted elimination of *CRPA*. The tests carried out *in vivo* using a full-thickness skin defect model in mice infected with *CRPA* showed that the ChMA–AgNPs hydrogel had a significant effect on the purulent exudation of wound sites. It also enhanced the rate of re-epithelialization, improved orderly collagen fiber deposition and neovascularization and successfully suppressed the expression of inflammatory mediators, including TNF-α and IL-6, thereby healing the wounds adeptly on postoperative day 14. Overall, the ChMA–AgNPs chemotactic antibacterial hydrogel designed in the present study demonstrates encouraging prospects of clinical use because it offers a novel therapeutic approach for managing *CRPA*-infected wounds *via* the synergistic effect of active chemotaxis-assisted bactericidal action and wound healing.

Received 20th March 2026,
Accepted 19th May 2026

DOI: 10.1039/d6bm00417b

rsc.li/biomaterials-science

1. Introduction

Carbapenem-resistant *Pseudomonas aeruginosa* (CRPA) is one of the most dangerous organisms implicated in clinical wound infections. This strain can exhibit a complicated spectrum of mechanisms of resistance and an increased colonizing ability, which initiates chronic, continuously invasive wound infections that significantly extend the duration of the healing process and potentially lead to life-threatening systemic complications.[1] Antibiotic therapy is still considered the first choice in the clinical procedures of *CRPA* infections. However, the overuse of antimicrobial agents stimulates the development of resistant phenotypes faster.[2] Traditional antimicrobial dressings lack antimicrobial efficacy, targeting efficiency, and the capability of eliminating biofilms as they are largely dependent on passive contact-killing processes, and therefore, they cannot meet clinical care demands adequately. As a result, the creation of new biomaterials combining active targeting, high-efficiency antimicrobial action, and wound restorative properties will be a crucial step in overcoming the problems that *CRPA* infections pose (Scheme 1).

Chemotactic antimicrobials are considered future active targeting modalities that take advantage of bacterial chemotaxis to specific chemical attractants as a means of achieving directed

---

[a] *Department of Burn, Plastic and Aesthetic Surgery, Guangxi Key Laboratory of Molecular Medicine in Liver Injury and Repair, the first Affiliated Hospital of Guilin Medical University, Guilin, 541001 Guangxi, China. E-mail: gongzhenyudoc@126.com, LSC526@126.com*

[b] *Institute of Burn Research, State Key Laboratory of Trauma and Chemical Poisoning, Southwest Hospital, The Third Military Medical University (Army Medical University), Chongqing 400038, China*

[c] *Department of Burn and Plastic Surgery, the First People's Hospital of Chenzhou, University of South China, Chenzhou, 423000, China. E-mail: czyyxxs@126.com*

†Xinxin Su and Morui Gui: these authors contributed equally to this work.

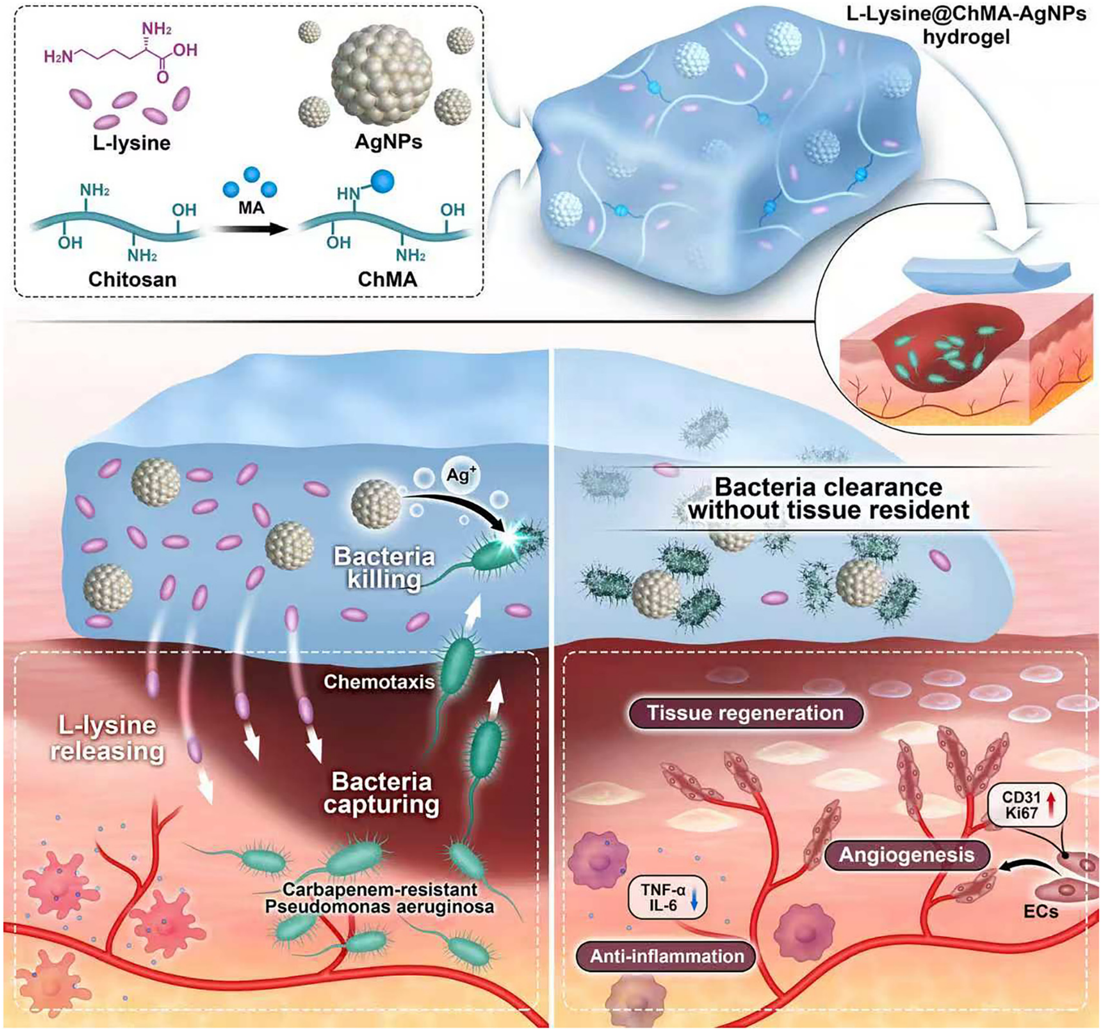

Scheme 1 Schematic of the synthesis and application of the ChMA–AgNPs hydrogel.

recruitment and localized microbial killing, thus providing new opportunities for the management of drug-resistant bacterial infections. Our group's prior research has revealed that the use of L-lysine, an optimal chemotactic compound optimized for *Pseudomonas aeruginosa* (*PAO1*), can induce directed motility in the reference strain *PAO1* as well as develop a highly efficient bactericidal system in the presence of L-lysine.[3] However, there are clinically resistant isolates, which exhibit significant biological variants of the standard strain, and the chemotactic specificity and mechanism of action of L-lysine against the clinically resistant strains like *CRPA* are also poorly understood. In addition, the regulatory processes that determine the speed and directionality of bacterial chemotaxis as well as the effect of charge state of chemotactic solutions on chemotactic behavior deserve thorough research.

Chitosan due to its high biocompatibility, biodegradability and natural antimicrobial property has been largely utilized in wound repair materials.[4,5] However, the low solubility of native chitosan in aqueous solutions and the difficulty in crosslinking and shaping impede the clinical translation and utilisation of chitosan significantly. Chitosan is an acid-soluble polysaccharide. After modification with methacrylic anhydride, methacrylated chitosan is formed with rapid UV-triggered crosslinking capability, which substantially improves the processability and mechanical stability of the resultant hydrogel material.[6] Silver nanoparticles (AgNPs) can be regarded as a classical, broad-spectrum antimicrobial agent possessing a great bactericidal effect against various drug-resistant bacteria, including *CRPA*.[7] Nonetheless, the biosafety of AgNPs depends on their concentration negatively: on the one hand, high concentrations can easily cause tissue toxicity and inflammatory reactions, and on the other, low concentrations cannot provide effective antimicrobial effects.[8]

Recently, DNA-inspired double-crosslinked self-healing hydrogels have been developed to synergistically regulate the wound microenvironment by integrating antibacterial, anti-inflammatory, and pro-angiogenic functions.[9] Furthermore, pH-responsive microneedle hydrogels have enabled real-time pH monitoring and intelligent drug release for diabetic wound care.[10,11] In addition, deer antler decellularized extracellular matrix (dECM) hydrogels combined with Mg–EGCG nanocomposites exhibit enhanced antibacterial, antioxidant, and pro-angiogenic activities for chronic wound repair.[12] Despite these advances in multifunctional hydrogels, challenges remain in balancing antimicrobial efficacy and biosafety. Therefore, achieving a favorable balance between the antibacterial performance and biosafety of silver nanoparticles (AgNPs) *via* stable loading, while endowing hydrogels with versatile functionalities, represents the ultimate goal to address the key challenges of composite antibacterial materials in this study.

To address the clinical challenges in treating wounds infected with carbapenem-resistant *Pseudomonas aeruginosa* (CRPA), this study verified the specific chemotactic effect of L-lysine on clinically isolated CRPA strains and constructed a methacrylamide chitosan composite hydrogel loaded with L-lysine and silver nanoparticles. The hydrogel's *in vitro* antibacterial performance, biosafety, and *in vivo* therapeutic efficacy in infected wounds were systematically evaluated. This study provides a novel active chemotactic antibacterial strategy for the clinical intervention of CRPA-infected wounds.

2. Materials

Chitosan (CS, low molecular weight) and methacrylic anhydride (≥98%, containing 2000 ppm topanol A as an inhibitor; MW = 154.16) were obtained from Sigma-Aldrich (Shanghai, China). Lithium phenyl(2,4,6-trimethylbenzoyl)phosphinate (LAP, MW = 296.23, purity >99.8%) was obtained from Engineering for Life Intelligent Equipment Co. (Suzhou, China). L-Lysine, L-alanine, L-glycine, L-lysine, L-proline, L-serine, and L-histidine (all amino acids have a purity >99%) were purchased from Aladdin Reagent Co. (Shanghai, China). Prepared plate media were obtained from Hope Bio-Technology Co. (Qingdao, China). Collagenase type I (360 U mg^{-1} DW) was obtained from Diamond Biotechnology Co. The Calcein/PI Cell Viability/Cytotoxicity Assay Kit, Antifade Mounting Medium with DAPI, and phosphate-buffered saline (PBS, 1×, premixed powder) were obtained from Beyotime Biotechnology Co. The SYTO 9/PI Live/Dead Bacterial Double Stain Kit was obtained from MKbio Co. Ultrapure water was obtained from Heal Force water purification systems. The Cell Bank of Typical Culture Collection, Chinese Academy of Sciences (China), supplied the NIH-3T3 fibroblasts. *Carbapenem-resistant P. aeruginosa* (*CRPA*), *Methicillin-resistant Staphylococcus aureus* (*MRSA*) and *Carbapenem-resistant E. coli* (*CREC*) strains were provided by the microbiological laboratory of the Department of Burns, Southwest Hospital, First Affiliated Hospital of Army Medical University (Chongqing, China). Male BALB/c mice (6–8 weeks, 20–25 g) and Sprague–Dawley rats (6–8 weeks, 200–220 g) were provided by the Third Military Medical University, Laboratorial Animal Department. All animal experiments were conducted according to protocols approved by the ethics committee of the First Affiliated Hospital of Army Medical University under approval number AMUWEC20224129.

3. Methods

3.1. Synthesis of methacrylamide chitosan

Methacrylamide chitosan (ChMA) was synthesized according to a previously published procedure with some modifications.[13,14] First, low-molecular-weight chitosan powder (3%, w/v) was dissolved in an acetic acid solution (2%, v/v) overnight at room temperature. Methacrylic anhydride was added to the solution at a mole ratio of 0.4 with respect to one mole of chitosan repeating unit and reacted at room temperature for 3 h. Finally, the sample was dialysed against deionized water for 5 days and lyophilized to obtain ChMA. The sample was kept at −20 °C for further use.

3.2. Synthesis of the ChMA–AgNPs hydrogel

The lyophilized ChMA was dissolved in deionized water (2%, w/v). After complete dissolution, a AgNPs dispersant (1 mg mL^{-1}) was added and thoroughly mixed. L-Lysine (10 mM) and lithium phenyl(2,4,6-trimethylbenzoyl)phosphinate (LAP, 0.5%, w/v) were sequentially added to prepare the ChMA–AgNPs hydrogel pre-gel solution. Gelation was induced by UV irradiation for 5 minutes to obtain the ChMA–AgNPs hydrogel. Direct addition of 0.5% LAP to the 2% ChMA solution, followed by UV irradiation for 5 minutes, induced gelation, yielding the ChMA hydrogel.

3.3. *In vitro* chemotaxis assay

To evaluate bacterial chemotaxis, three experiments were conducted: soft-agar motility assay, capillary quantitative chemotactic method, and agar titration tests.[15,16] The following reagents were prepared: L-alanine, L-glycine, L-lysine, L-proline, L-serine, L-histidine, and PBS, all sterilized using a 0.22 micron filter. Following previous reports, motility agar plates were prepared using 0.3 g of yeast, 1 g of peptone, 0.25 g of agar powder, 0.5 g of sodium chloride, and 300 mL of deionized water.[17] After autoclaving, the hot solution was poured into 100 mm Petri dishes. Control plates contained 15 mL agar solution per plate. Experimental plates contained 3 mL chemotactic solution and 12 mL agar per plate. Plates were cooled for 4 hours and stored at 4 °C. A 6 mm diameter circle of autoclaved, dry filter paper was placed at the center of each agar plate. Then, 5 μL inoculum of bacterial suspension was added, and the plates were incubated at 37 °C with 5% CO_2 for 12, 16, 20, and 24 hours, with photographs taken at each time point. The colony area was measured using a colony counter. To further evaluate the effect of chemotactic charge on flagellar growth in *CRPA* colonies, we repeated the motility agar plate colony spread assay using electrically neutral *N*-α-acetyl-L-lysine as a control group.

Following previous reports,[18,19] briefly, the micro-capillary tubes (capacity: 20 μL; length: 20 cm; inner diameter: 0.8 mm) were divided into 8 groups (L-alanine, L-glycine, L-lysine, L-proline, L-serine, L-histidine, PBS and control). One end of the microcapillary tube was inserted into the chemoattractant solution to draw the liquid to 10 μL high, and the other end was sealed to maintain the liquid level. The liquid end of the tube was inserted again into the bacterial suspension. After 30 minutes, the test tube was removed and rinsed to get rid of any residual bacteria adhering to the tube walls. Following 10^2 dilution, 100 μL of the bacterial suspension was taken and spread evenly onto a nutrient agar plate. The number of colonies on the plate was counted after the bacteria were cultured overnight at 37 °C.

Chemotaxis involves both directionality and motility.[20] To focus on observing the direction of movement, we increased the agar concentration to minimize the influence of movement speed. Motility agar plates were prepared using 0.3 g of yeast, 1 g of peptone, 0.4 g of agar powder, 0.5 g of sodium chloride, and 300 mL of deionized water. After autoclaving, the hot solution was poured into 100 mm Petri dishes. After cooling for 4 hours, 6 mm-diameter dried filter paper discs were placed at approximately one-third intervals around the agar plate, each of which was inoculated with 5 μL of bacterial suspension and the candidate chemotactic solution, respectively, followed by incubation at 37 °C for 24 and 48 hours. The direction of colony growth was observed by photographing them.

3.4. Wound healing assay in BALB/c mice

A full-thickness skin wound model was established in male BALB/c mice *via* intraperitoneal pentobarbital sodium anaesthesia. The mice were randomly divided into four groups: the blank group (noninfected), the ChMA group, the ChMA–AgNPs group, and the control group (after infection, only gauze coverage was applied without any other treatment). After hair removal, two 6 mm full-thickness wounds were created on the dorsal skin. The wound sites received 4 μL of *CRPA* (1×10^7 CFU mL^{-1}). Hydrogels were applied according to group assignments and covered with sterile gauze. After dressing changes, photographs were taken on day 0, 3, 7, and 14. The tissue samples were fixed in 4% polyformaldehyde, paraffin-embedded, and stained with H&E and Masson's trichrome. The epithelial length was measured by two independent observers using the ImageJ software. After 14 days, major organs (liver, heart, spleen, kidney, and lung) were collected for H&E staining.

3.5. Data analysis

The experimental data were analysed using the Origin 2021 and Adobe Illustrator 2023 software packages. The results are presented as mean ± standard deviation (SD). Statistical significance between groups was determined through one-way ANOVA with the Tukey/Holm-Šidák *post hoc* tests. The differences were considered statistically significant at $P < 0.05$ (marked with *), highly significant at $P < 0.01$ (marked with **), and extremely significant at $P < 0.001$ (marked with ***). Nonsignificant differences are denoted as ns.

4. Results and discussion

4.1. Screening of chemotactic agents for *CRPA*

Based on a preliminary amino acid test of activating the chemotaxis of *PA01*, we identified L-lysine as a potent chemotactic attractant and further developed a corresponding antibacterial system.[3] This study discusses whether this chemotactic agent can act against clinically resistant strains. To do this, we tested the soft-agar motility assay to assess the chemotactic effects of L-alanine, L-glycine, L-lysine, L-proline, L-serine, L-histidine, and PBS on three common drug-resistant strains: *CRPA* (Fig. 1A), *CREC* (Fig. 1B), and *MRSA* (Fig. 1C and Fig. S1C). Statistical analysis of colony spread areas at 12, 16, 20, and 24 hours shows that L-lysine maintains the best chemotactic activity against *CRPA*, with significantly larger spread areas than that of other groups (Fig. 1F and Fig. S1A). However, when *CREC* plates were used, the bacteria growth rate increased at a higher rate and almost the entire plate was covered after 12 hours. Chemotactic response towards various amino acids did not have significant differences and no apparent benefit of L-lysine was recorded (Fig. 1G). In the meantime, *MRSA* showed no noticeable spreading during the 24-hour observation period (Fig. S1B), which is directly linked to the absence of a motile flagellar system. These results imply that L-lysine would be very appropriate for use as a chemotactic agent in *CRPA* but not in *CREC* or *MRSA*.

Based on the above-mentioned experimental results, we performed a capillary assay (Fig. 1D) to quantitatively evaluate the chemotactic attraction of L-lysine to *CRPA*. At 30 minutes, the number of bacteria attracted by L-lysine was significantly higher than that attracted by other chemoattractants (Fig. 1H), indicating that CRPA preferentially migrated toward the L-lysine solution under identical experimental conditions. In addition, we conducted a central pore assay to quantify the migration distance of bacteria induced by L-lysine (Fig. S12A). During continuous observation over 24 hours, the outward crawling trend of bacterial colonies from the central pore was notably stronger on the side with the L-lysine solution than that of the PBS control group. We measured the distance from the central pore colony to the farthest migrating colony at 12, 16, 20, and 24 h, and the results showed that the migration distance toward the L-lysine solution was significantly greater than that toward the PBS solution, with a statistically significant difference (Fig. S12B). Collectively, the results of these experiments consistently demonstrate that L-lysine exerts a clear chemotactic effect on CRPA, inducing directional migration of the bacteria.

To further examine its directional movement, we performed agar drop assays on plates with higher agar concentrations (Fig. 1E). Our distinct colony morphologies were observed after 48 hours of colony growth. Bacterial colonies on plain agar plates were almost circular, indicating that they diffused randomly without any directional preference. Colonies, conversely, on L-lysine plates displayed a circular right side with an outgrowth towards the source of L-lysine. The colonies also displayed greater overall leftward growth, with the left edge closer to the L-lysine source (Fig. 1I). These observations demonstrate that CRPA exhibits a directional response to L-lysine.

In summary, we demonstrated the superiority of L-lysine over *CRPA* in terms of both speed and direction of chemotaxis. Additionally, we observed that in the soft-agar motility assay,

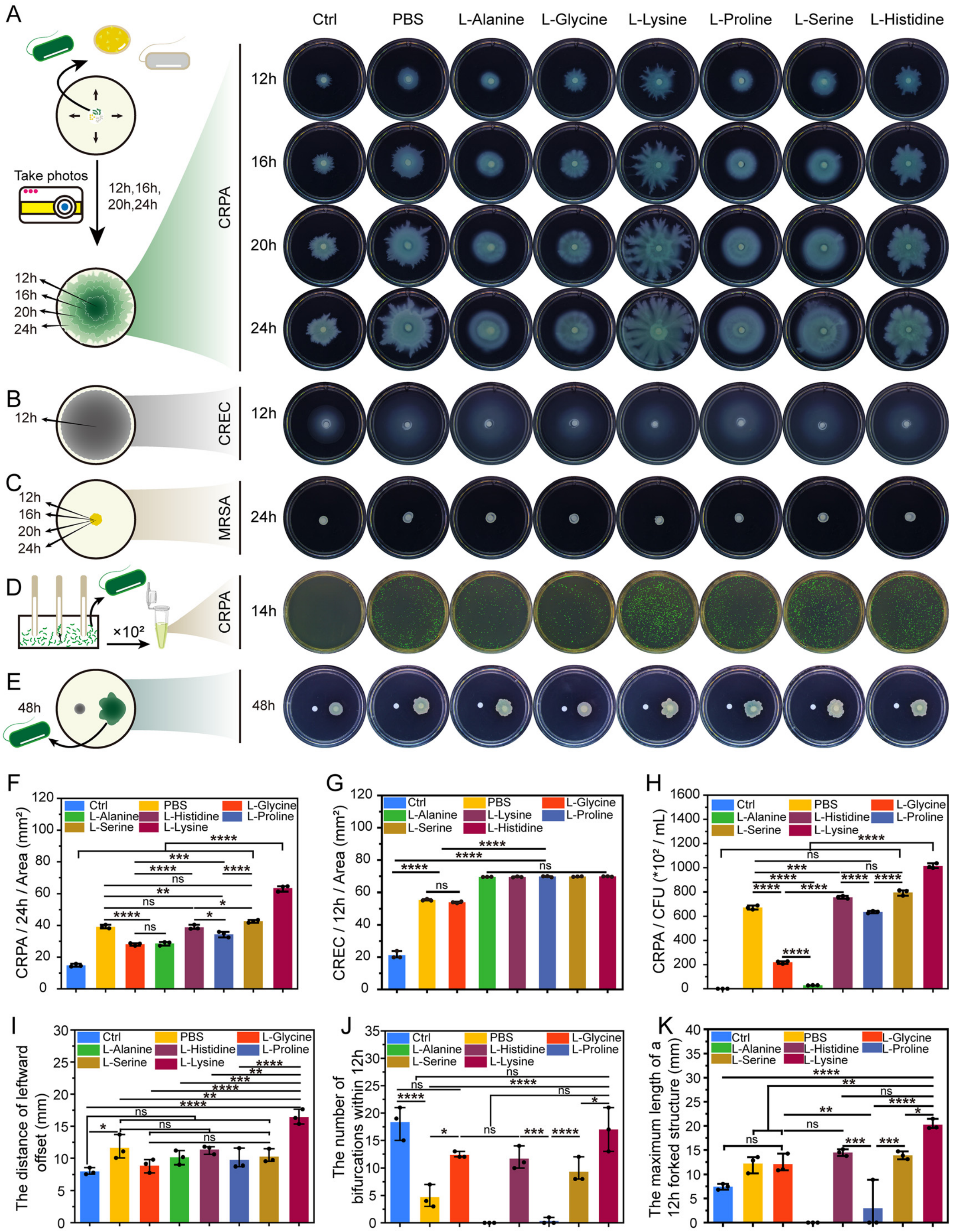

Fig. 1 *In vitro* chemotaxis of *CRPA*, *CREC*, and *MRSA*. (A) Schematic and representative results of the *CRPA* soft-agar motility assay. (B) Schematic of the *CREC* concentric circle experiment and representative results after 12 hours. (C) Schematic of the *MRSA* concentric circle experiment and representative results after 24 hours. (D) Schematic of the capillary quantitative chemotactic method and the representative plate diagram. (E) Schematic of the *CRPA* agar titration tests and the representative results after 48 hours. (F) Statistical analysis of the 24-hour chemotactic colony area formed by *CRPA* in response to different chemotactic agents. (G) Statistical analysis of the diffusion colony area produced by *CREC* under different chemotactic agents. (H) Statistical analysis of the chemotactic bacterial counts formed by *CRPA* in response to different chemotactic agents after 30 minutes. (I) Statistical analysis of the primary tendril length induced by different chemotactic agents in *CRPA* at 48 hours. (J) Statistical analysis of the tendril number induced by different chemotactic agents in *CRPA* at 12 hours. (K) Statistical analysis of the longest tendril at 12 hours in the soft-agar motility assay comparing the effects of charge ($n \geq 3$, $P < 0.05$ (*), $P < 0.01$ (**), $P < 0.001$ (***) and ns: nonsignificant difference).

colonies on L-alanine, L-glycine, L-proline, and L-serine plates exhibited circular or near-circular colonies, whereas colonies on PBS, L-lysine, L-histidine, and pure agar plates displayed irregular shapes with branching at the periphery and tendril-like extensions. We statistically analyzed the number of branches and the length of primary branches across different plates (Fig. 1J and K). Among these, L-lysine plates exhibited the most pronounced branching phenomenon, characterized by the highest number of branches and the longest tendril patterning. Previous studies have shown that bacterial flagella are associated with charge properties.[21,22] Divalent cations influence the production of proteins and surface-active substances during bacterial growth, ultimately affecting motility.[23] As basic amino acids, L-lysine and L-histidine carry positive charges, while L-alanine, L-glycine, L-proline, and L-serine are neutral amino acids with no charge. This aligns with the previous findings.

Future research focuses on the relationship between the growth of bacterial colonies and their charges. We also reiterated the soft-agar motility assay with the neutral *N*α-acetyl-L-lysine control group to confirm the presence of the branching effect due to the charge of L-lysine. Colonies on the fit of L-lysine plates were shown to branch and bear tendrils. Conversely, the colonies on *N*α-acetyl-L-lysine plates had slight branching in the initial stages with rather short tendrils. There was gradual evidence of the colonies becoming more circular in their outer edges, and it all soon rounded off (Fig. 2A). Using colony area (Fig. 2B), we could find that colony area on *N*α-acetyl-L-lysine plates was very small compared to the L-lysine plates. This implies that when the positive charge interaction was lost, it slowed the colony spreading velocity indicating the lessening of its motility.

Drug resistance evolution induces global reorganization of the transcriptome. Comparative transcriptome analysis of 15 functional sub-modules between the standard strain and the drug-resistant strain revealed that the acquisition of drug resistance is accompanied by extensive metabolic and functional reorganization (Fig. 2C and D). The Global Expression Radar indicated that the drug-resistant strain exhibits significant expression expansion in modules related to energy metabolism (such as glycolysis and ATP synthase), fatty acid synthesis, and rhamnolipid regulation. In contrast, the standard strain demonstrates distinct distribution characteristics in certain flagellar motility modules (such as Basal body and Hook) compared to the drug-resistant strain, suggesting essential differences in survival strategies between the two groups.

A fine regulation and "energy-saving" strategy of the flagellar assembly network was developed. To explore the microscopic changes in the motility system, this study constructed a flagellar assembly gene co-expression network based on the physical structure. The results showed that the genes encoding the core components of flagellar filaments, fliC and fliD, were significantly downregulated ($\log2FC < -10$) in *CRPA* (Fig. 2E). Although the basal body and hook genes maintained a certain expression correlation, the coordinated downregulation of distal accessory genes reflected the active "downsizing" of high-energy-consumption motility organs in *CRPA*. At the same time, some Type IV pilus genes showed an upward trend or maintained their expression, indicating that *CRPA* may switch from a swimming mode to a more energy-efficient surface attachment or crawling mode.

Carbon flux reprogramming drives the biosynthesis of rhamnolipids. Through the in-depth analysis of the metabolic pathway, we found that *CRPA* supports their defense system by optimizing carbon source allocation. Quantitative results showed that the core genes rhlA and rhlB, as well as the regulatory genes rhlI and rhlR, involved in rhamnolipid synthesis were significantly upregulated in *CRPA* (Fig. 2G and H). Gene Set Phenotypic Landscape (Fig. 2I) demonstrates that the evolution of resistance follows a specific trade-off mechanism, where by reshaping the transcriptional network, the strain gains stronger metabolic adaptability and population defense capabilities while sacrificing some traditional motility characteristics. The metabolic carbon flux map further revealed a clear cascade effect: enhanced glycolysis, TCA cycle, and fatty acid synthesis pathways in *CRPA* produced sufficient acetyl–CoA (Fig. 2F). These metabolic intermediates were largely channeled to the rhamnolipid synthase module through hubs such as β-OH fatty acids, achieving flux reprogramming from primary metabolism to secondary pathogenic metabolism.

4.2. Characterization of hydrogels

The earlier research studies have indicated that chitosan is antibacterial and biocompatible, but its acid solubility limits its applications.[24–26] In the current study, we added methacrylamide moieties to form a water-soluble derivative (ChMA) without altering the properties of the core structure of chitosan. Given the high toxicity of *CRPA*, we selected AgNPs as the antimicrobial agent. In this regard, we created a hydrogel dressing which comprises L-lysine to actively attract bacteria, AgNPs presented the main antimicrobial factor in the hydrogel, and ChMA shows synergistic action in the wound bed. This is a chemotactic antimicrobial hydrogel dressing that should be used in the treatment of invasive wound infection that is refractory.

We verified ChMA by ^{1}H NMR, and the peaks at 5.19 and 5.41 ppm represented the ethylene matrix subsignal. The ^{1}H-NMR spectrum of natural chitosan showed no chemical shifts in the range of 5.0–5.5 ppm, which demonstrated the successful preparation of ChMA.[27–29] After UV crosslinking, all the formulations formed stable gels (Fig. 3A).

Before the gelation process, the individual component solutions were subjected to Fourier transform infrared (FTIR) analysis and cured hydrogel (Fig. 3B and C). The absorption peaks of the pure L-lysine solution, the ChMA solution, and the ChMA–AgNPs mixture before gelation were similar, indicating that L-lysine and AgNPs were uniformly dispersed within the ChMA solution without chemical interaction. The infrared absorption spectra of the ChMA hydrogel and ChMA–AgNPs hydrogel were similar following the crosslinking by UV-light, which once again indicated that in this system, the L-lysine and AgNPs did not engage in any new chemical reactions with

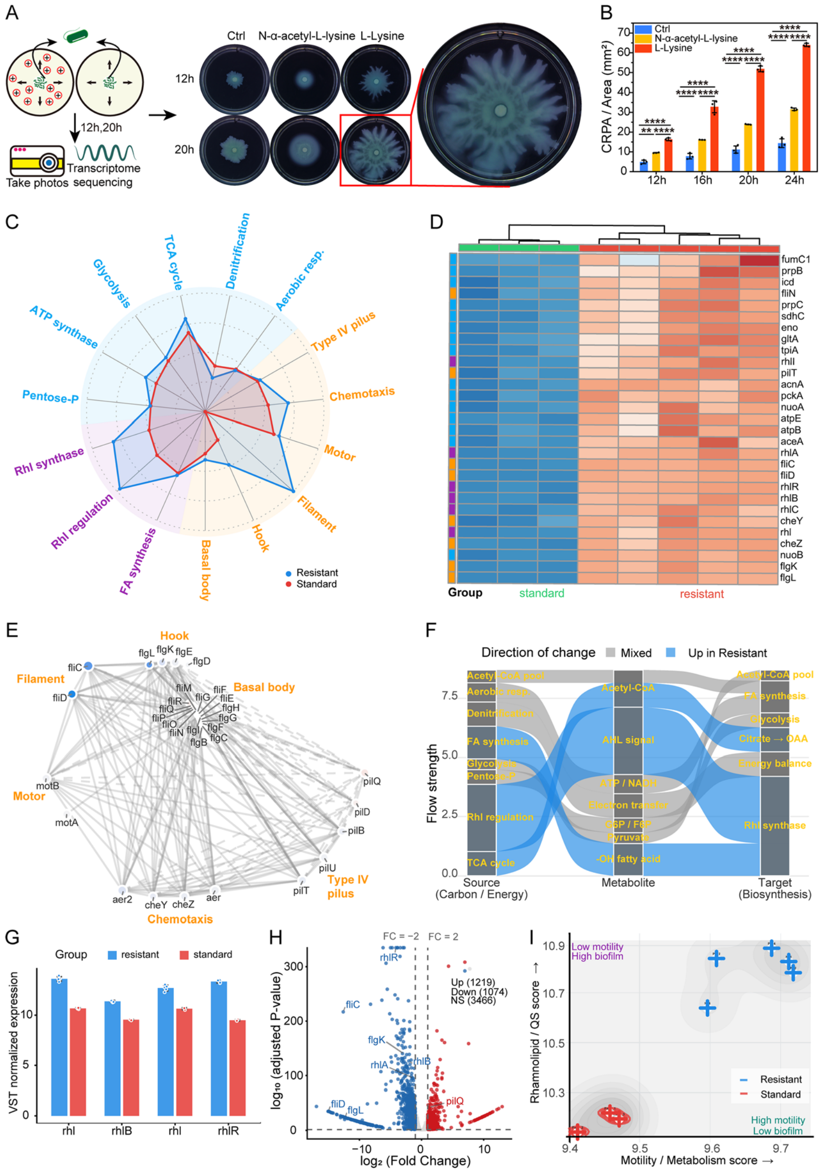

Fig. 2 Analysis of global expression and the metabolic landscape of *CRPA* and standard strains. (A) Schematic and representative image of the soft-agar motility assay comparing charge effects. (B) Statistical analysis of the colony area in the soft-agar motility assay comparing charge effects. (C) Global expression radar showing the expression level comparison of 15 functional sub-modules between *CRPA* (blue) and standard strains (red). The outward expansion of the blue line represents a significant upregulation in the expression levels in *CRPA* in pathways such as chemotaxis, flagellar growth (filament/hook/basal body), and Rhl synthesis and regulation. (D) Heatmap of differentially expressed genes. Each row in the map represents a specific gene, and each column represents a sample. The evolutionary tree clustering at the top divides the samples into two major categories: standard (green) and resistant (red). The color bar on the left represents the functional classification of genes: orange represents flagellar motility, purple represents rhamnolipid, blue represents metabolism, and gray represents others. The color scale on the right represents the relative level of gene expression: red indicates high expression, blue indicates low expression, and the numerical value is the normalized *Z*-score. (E) Metabolic carbon flow of rhamnolipid biosynthesis. The blue pathways represent enhanced metabolic flows in *CRPA*, highlighting the increased contributions of acetyl–CoA, pyruvate, and fatty acid (FA) synthesis to the final Rhl synthase. The color of each node indicates the $\log_2$ fold change ($\log_2$FC) in gene expression in the resistant strain compared with the standard strain (blue: downregulated and red: upregulated). The size of each node is proportional to the $\log_{10}$-transformed base mean expression level of the gene. Gray lines represent the co-expression relationships between genes. (F) Flagellar assembly gene network depicting the co-expression relationships among flagellar-related genes (such as fli, flg, and mot). The color of the nodes represents $\log_2$ FC (fold change), with blue indicating significant upregulation in *CRPA*; the size of the nodes represents the basal expression level of the gene. (G) Rhamnolipid core gene expression quantitatively comparing the VST normalized expression levels of four key genes: rhlA, rhlB, rhlC, and rhlR. The results show that the expression of these core synthesis genes in *CRPA* (blue) is significantly higher than that in standard strains (red). (H) Volcano plot of differentially expressed genes. Each point in the plot represents a gene. The horizontal axis represents the $\log_2$-transformed fold change, and the vertical axis represents the $\log_{10}$-transformed adjusted *P*-value. (I) Gene set phenotypic landscape displaying the distribution of strain scores in the two dimensions of "motility/metabolism" and "rhamnolipid/quorum sensing (QS)" through a scatter plot. The standard strains are located in the lower left corner (high motility, low biofilm), while the *CRPA* cluster in the upper right corner (low motility, high biofilm) ($n \geq 3$, $P < 0.05$ (*), $P < 0.01$ (**), $P < 0.001$ (***) and ns: nonsignificant difference).

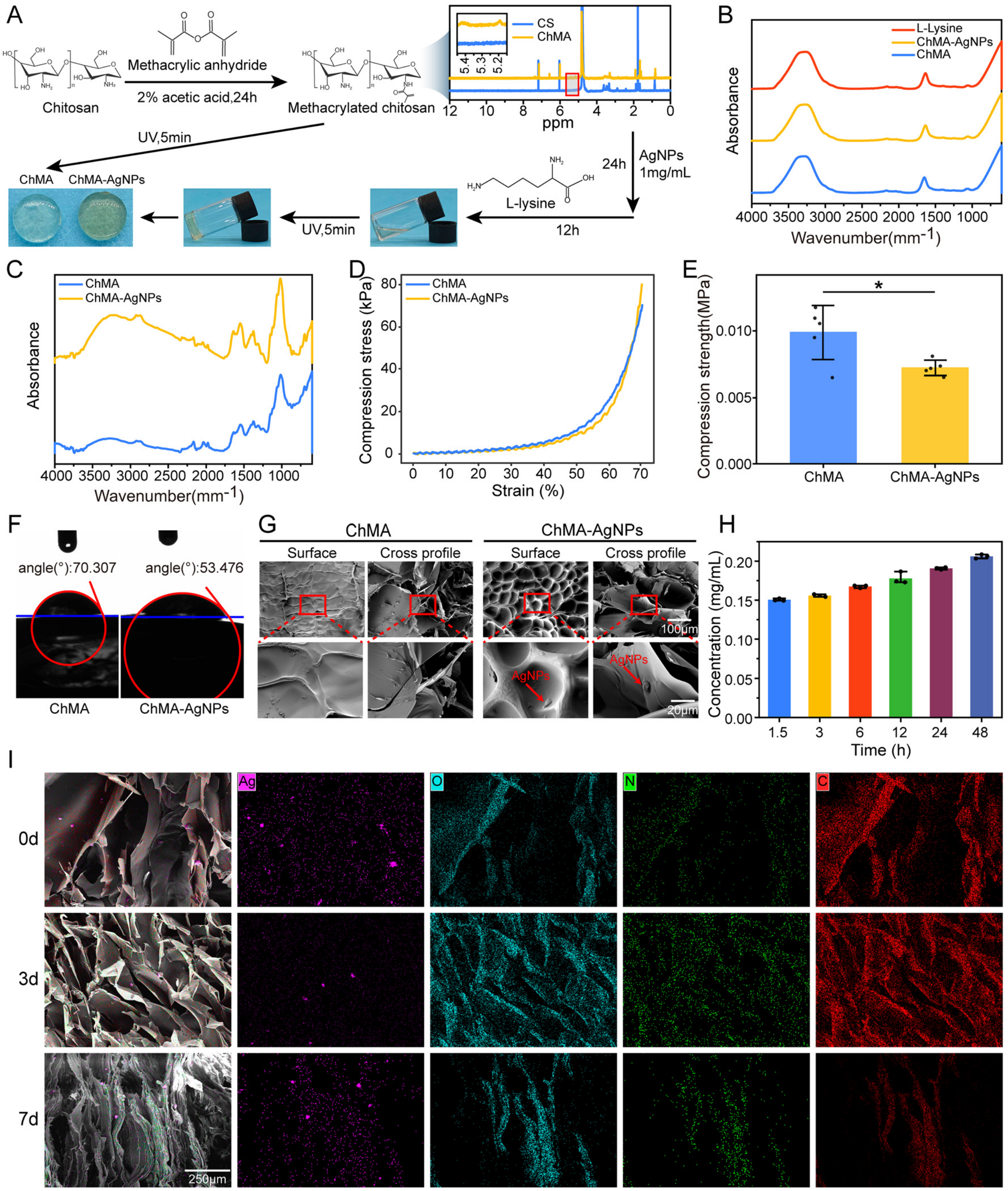

Fig. 3 Synthesis and characterization of the hydrogel composites. (A) Synthesis of hydrogel composites. (B) FTIR spectra of different components of the hydrogel in the liquid state. (C) FTIR spectra of the composite hydrogels with different contents. (D and E) Compressive strengths of the composite hydrogels with varying contents. (F) Contact angle images of the ChMA and ChMA–AgNPs hydrogels. (G) SEM images of the ChMA and ChMA–AgNPs hydrogels. (H) Release of L-lysine in the hydrogels. (I) Elemental analysis of the hydrogels (0, 3, and 7 days) (*n* ≥ 3, $P < 0.05$ (*), $P < 0.01$ (**), $P < 0.001$ (***) and ns: nonsignificant difference).

ChMA but were simply physically embedded in the ChMA network. During compression testing (Fig. 3D and E), stress–strain curves of the ChMA hydrogel and ChMA–AgNPs hydrogel were close to each other, and there were negligible differences in compressive strength. This further shows that AgNPs and L-lysine were loaded and immobilized successfully, which maintained the initial mechanical characteristics of the basic hydrogel.

Subsequent water contact angle analysis revealed a value of 70.307° for the ChMA hydrogel and 53.476° for the ChMA–AgNPs hydrogel (Fig. 3F). This suggests that the hydrophilic activity of the hydrogel of the ChMA–AgNPs is high, which is more applicable in a wound setting. The scanning electron microscopic (SEM) images (Fig. 3G) reveal the microstructure of the hydrogels. The cross-section and surface of the ChMA hydrogel seem clean and devoid of attachments. The surface of the ChMA–AgNPs hydrogel exhibits irregular particles encapsulated within an outwardly protruding contour. It is evident that there are distinct AgNPs in the cross-section. These results confirm that AgNPs are well-embedded within the ChMA network instead of being exposed on the hydrogel surface; therefore, the adverse effects on the tissue are minimal.

The chemotactic effect of the hydrogel is based on the release of L-lysine. To clarify its release profile, we generated a standard release curve (Fig. S2A) and quantified the release at 1.5, 3, 6, 12, 24, and 48 hours (Fig. 3H). The results indicate that L-lysine is slowly released from the hydrogel, forming a centrally diffusing concentration gradient as expected. This enables chemotaxis toward *CRPA*. Silver exposure to tissues can cause severe side effects. Therefore, we freeze-dried ChMA–AgNPs hydrogels after immersing them in physiological saline for 0, 3, and 7 days, followed by quantitative SEM scanning for silver and routine scanning for carbon, hydrogen, and oxygen elements. Quantitative analysis of the silver content was performed (Fig. S2B), and the results demonstrated no statistically significant difference in silver content among hydrogels with varying immersion durations. The SEM images of labeled element distribution visually revealed the distribution sites and concentrations of silver (Fig. 3I).

In addition, we performed XPS analysis on the ChMA–AgNPs hydrogel after immersion in normal saline for 0, 3, and 7 days (Fig. S13). The silver signal was weak or even undetectable, which is due to the extremely low silver loading on the hydrogel surface, close to or below the instrument's detection limit. Combined with the results in Fig. 3I, it was confirmed that silver nanoparticles are firmly encapsulated within the hydrogel matrix, with minimal silver release during immersion. Based on these findings, the antibacterial mechanism of the hydrogel is clarified to be dominated by the synergistic effect of contact killing and the near-field effect produced by surface-enriched silver nanoparticles: trace, highly dispersed silver active sites on the material surface directly disrupt bacterial cell membranes and inhibit their physiological metabolism; meanwhile, locally enriched silver nanoparticles generate a near-field enhancement effect, enabling efficient antibacterial activity even at extremely low silver loadings, with negligible adverse effects on skin tissue.

ChMA hydrogels have high absorption and swelling of water. In situations where the amount of wound exudate is high, full swelling also causes a displacement effect which obstructs wound contraction. Adding L-lysine and AgNPs decrease your swelling, which allows your exudates to be taken up without a big displacement (Fig. S2C). Additionally, the hydrogel has great water retention ability (Fig. S2D). The ChMA–AgNPs hydrogel maintained a water retention rate of 54.63% after 24 hours, contributing to the maintenance of the moist environment required for wound healing. The degradation of the hydrogels was examined under physiological condition simulation (37 °C, collagenase type I). It was found that the ChMA–AgNPs hydrogel maintains 41.18% of its structure after day 7 (Fig. S2E). Throughout the degradation process, both hydrogels maintained structural stability, thereby providing prolonged antimicrobial protection at the wound site. From a clinical perspective, it helps in the acute and chronic or difficult-to-heal wounds to limit the number of dressing changes, secondary trauma, and patient discomfort.

4.3. *In vitro* antimicrobial evaluation

AgNPs lead to some wound tissue damage at high concentrations and little bactericidal action of low concentrations on *CRPA*. Hence, we prepared AgNPs with various concentrations and cross-linked them into a gel by using ultraviolet irradiations. The zone of inhibition analysis was used to determine the lowest effective concentration of AgNPs against the drug-resistant bacteria (Fig. 4A). In the case of *CRPA*, a AgNPs concentration of 1 mg mL^{-1} was finally chosen as the antimicrobial agent. The zone of inhibition assay was used to compare the antibacterial efficacies of the two hydrogels after gelation against three popular drug-resistant bacteria *CRPA*, *MRSA*, and *CREC* (Fig. S3A). The findings indicated that the ChMA–AgNPs hydrogel had a greater antibacterial ability than that of the ChMA hydrogel alone with the highest efficacy against *CRPA* and reduced efficacy against *CREC*.

To further investigate their antibacterial efficacy, we co-cultured the two hydrogel groups with three common drug-resistant bacteria. After 3, 6, 12, and 24 hours, the antibacterial efficacy was further evaluated by measuring the 600 nm absorbance values and colony-forming unit (CFU) counts (Fig. 4B, Fig. S3B). Statistical analysis revealed superior antibacterial activity of the ChMA–AgNPs hydrogel against *CRPA* (Fig. S3C), with significant differences observed at 3 h (Fig. S3F), 6 h (Fig. S3G), 12 h, and 24 h (Fig. 4C). The macrographs of residual bacterial colonies correlated with the statistical findings (Fig. S3H). The ChMA–AgNPs hydrogel exhibited acceptable antibacterial efficacy against *CREC* at 3 h (Fig. S3I) and 6 h (Fig. S3J), but its efficacy declined at 12 h. By 24 h, no statistically significant difference remained compared to the untreated control group (Fig. 4D and Fig. S3D). The macrographs of residual bacterial counts correlated with the statistical results (Fig. S3K). The ChMA–AgNPs hydrogel demonstrated superior antibacterial efficacy against *MRSA* compared to *CREC*, with activity sustained up to 24 hours (Fig. 4E and Fig. S3E, L). The macroscopic images of residual bacteria also corroborated the statistical findings (Fig. S3M).

Biofilms are surface-attached microbial communities encased in a self-produced extracellular matrix, supporting *CRPA* survival and virulence.[30,31] We next tested whether the ChMA–AgNPs hydrogel limits *CRPA* biofilm formation. Planktonic *CRPA* was seeded on the ChMA–AgNPs hydrogel surfaces and cultured for 24 h, followed by crystal violet staining. All groups formed mature biofilms visible to the naked eye (Fig. 4F). Following acetic acid dissolution and absorbance measurement (Fig. 4G), biofilm survival rates were further cal-

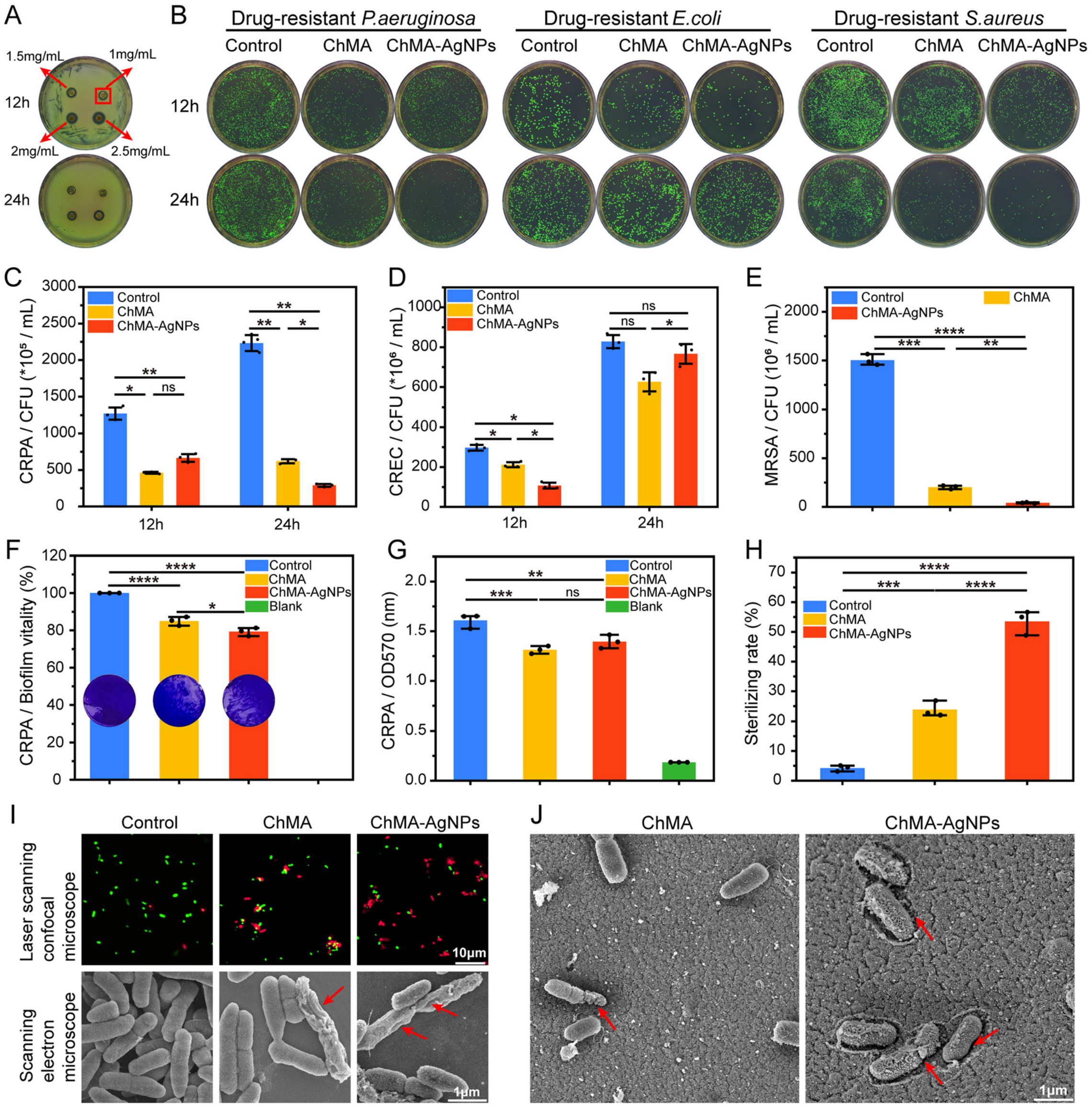

Fig. 4 *In vitro* antimicrobial evaluation of the hydrogels. (A) Representative images of the inhibition zone. (B–E) Standard antibacterial tablet and statistical analysis. (F) Planktonic bacterial biofilm activity. (G) Absorbance values of the crystal violet-stained planktonic bacterial biofilms at 570 nm. (H) Statistical analysis of live/dead (green/red) bacteria after treatment with different hydrogels. (I) Fluorescence photomicrographs and scanning electron microscopy images of live/dead (green/red) bacteria after treatment with different hydrogels. (J) Scanning electron microscopy images of the bacteria on the hydrogel surface ($n \geq 3$, $P < 0.05$ (*), $P < 0.01$ (**), $P < 0.001$ (***) and ns: nonsignificant difference).

culated. The results indicated that the inhibitory rate of the ChMA–AgNPs hydrogel against CRPA biofilm formation was less than 20%, indicating a limited inhibitory effect.

We also investigated the antimicrobial effects through the experimental measures of live/dead bacterial staining. The staining of SYTO9 can make all live bacteria emit green fluorescence, and the dead bacteria can emit red fluorescence through the propidium iodide staining. The rates of bactericides of the ChMA hydrogel group and ChMA–AgNPs hydrogel group were 23.85% and 53.49% after 3 h of coculture, respectively (Fig. 4H and I). To more intuitively observe the bactericidal effect, the morphological variation of bacteria was observed using SEM following 3 hours contacting exposure. CRPA proliferated in the control group as rod-shaped with clear flagella, and the bacteria in the ChMA hydrogel and ChMA–AgNPs hydrogel groups were significantly deformed, losing their rod-like shape with uneven surfaces. The number of bacteria per unit area also decreased significantly (Fig. 4I). Simultaneously, hydrogels incubated with a bacterial suspension for 3 hours were fixed and examined by SEM to observe bacterial distribution on the hydrogel surface (Fig. 4J). The deformation and low viability of bacteria were observed on the ChMA hydrogel surface. Contrastingly, bacteria on the surface of the ChMA–AgNPs hydrogel were not just deformed, but were embedded in the hydrogel. This indicates that bacteria were attracted by L-lysine and actively migrated into the hydrogel interior, enabling their synchronous removal with the material for more effective wound healing. Comprehensive evidence supports the potential application value of chemotaxis-assisted antimicrobial therapy in combating infections.

The present hydrogel system exhibits certain limitations, as its inhibitory rate against CRPA biofilm formation is less than 20%. It should be noted that the core design principle of this hydrogel is to achieve chemotactic capture and rapid killing of planktonic CRPA through L-lysine-mediated attraction, rather than directly intervening in key processes of biofilm formation such as quorum sensing, extracellular matrix secretion, or bacterial adhesion.[32,33] This material is intended for the early intervention of acute infected wounds. By reducing the number of motile planktonic bacteria at the initial stage of infection, it decreases the initial bacterial load for biofilm formation, instead of acting on preformed mature biofilms. In future research, biofilm-dispersing agents will be incorporated, including DNase I to degrade the eDNA backbone,[34] proteinase K to digest protein components,[35] and D-amino acids to interfere with the synthesis of extracellular polymeric substances (EPS),[36] to disrupt the biofilm structure. Multifunctional dressings possessing both chemotactic antibacterial activity and high-efficiency biofilm inhibition will be developed to adapt to more complex clinical scenarios of *CRPA* infections.

4.4. *In vitro* and *in vivo* biosafety

NIH-3T3 fibroblasts were used to determine the cytotoxicity of the hydrogel extracts. Live/dead cell staining kit showed a normal morphology with active proliferation in each of the groups (Fig. 5A). NIH-3T3 fibroblasts were found to be more than 96% viable (Fig. 5B). The results of the CCK-8 assay were comparable to those of the controls (Fig. 5C), and proliferation was not suppressed (Fig. 5D). Haemocompatibility testing revealed that the integrity of the erythrocytes was preserved,

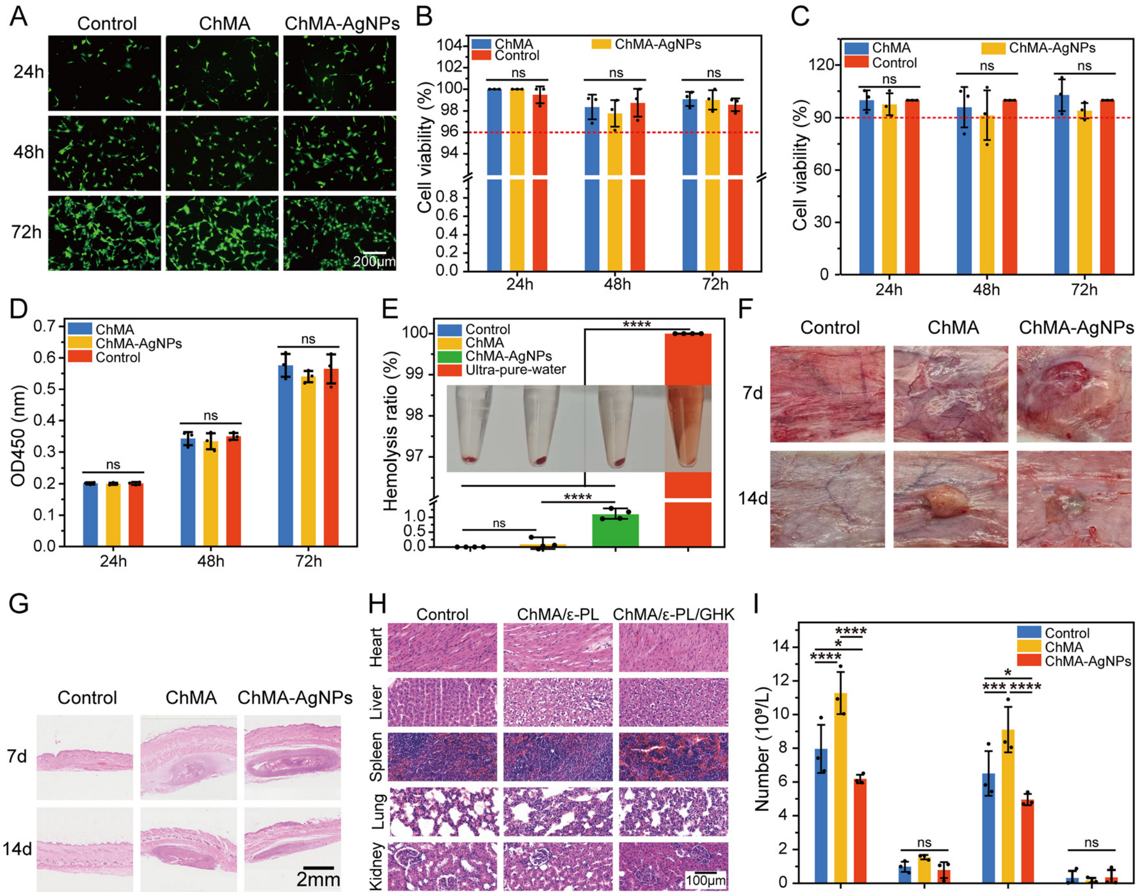

Fig. 5 *In vitro* and *in vivo* biocompatibility evaluation of the hydrogels. (A) Fluorescence staining of cells cultured with different sets of hydrogels for 1–3 d. The green colour represents live cells. (B) Quantitative analysis of relative fluorescence. (C and D) Cell viability and population growth of different fractions of hydrogels cocultured with 3T3 fibroblasts for 1–3 d. (E) Haemolytic activity and haemolysis rate in culture with different groups of hydrogels. (F) Photos of subcutaneous tissues in various groups of subcutaneous embedding. (G) Photos of H&E staining of the skin and subcutaneous tissues of rats. (H) H&E staining of the major organs of rats in various groups of subcutaneous embedding. (I) Numbers of inflammatory cells in routine blood samples from rats in various groups of subcutaneous embedding ($n \geq 3$, $P < 0.05$ (*), $P < 0.01$ (**), $P < 0.001$ (***) and ns: non-significant difference).

the supernatant of all the hydrogel groups was colourless and transparent, similar to the supernatant of the physiological saline control group, and the haemolysis rate was well below the accepted safety thresholds (Fig. 5E). These findings suggest that AgNPs at such concentration do not exert severe negative effects on the cells. Moreover, the AgNPs are enclosed in the ChMA network, and very low concentrations of the surface in the hydrogel are very low. To do additional evaluation, ChMA–AgNPs hydrogels were implanted subcutaneously into rats. The implants degraded gradually (Fig. 5F), and the histology failed to identify any abnormalities in the surrounding skin (Fig. 5G) or major organs (Fig. 5H). Besides, the ChMA–AgNPs hydrogel group showed similar results in complete blood cell counts to the untreated control group. Conversely, the group of hydrogel playing the role of ChMA displayed mild inflammatory reactions (Fig. 5I and S4). The overall findings show that ChMA–AgNPs hydrogels have high biocompatibility both *in vitro* and *in vivo*. We created a multifunctional hydrogel dressing through the optimization of composition ratios and chemical structural adjustments that allows blending cellular compatibility, hemocompatibility, and stability, rendering the dressing to be appropriate in the healing of wounds.

4.5. Wound healing evaluation in mice

We evaluated the efficacy *in vivo* using a murine full-thickness excisional wound model with *CRPA* infection (Fig. 6A). To minimize closure by contraction in line with human wounds, a white concentric ring 2 mm larger than the wound diameter was affixed on the wound as a splint against contraction. On day 3, the control group (after infection, only gauze coverage was applied without any other treatment) exhibited extensive purulent exudate with outward expansion of the wound surface, whereas the blank group (uninfected wound) and the ChMA–AgNPs group showed minimal exudate (Fig. 6B). By day 7, purulent secretions persisted in the control group, while other groups exhibited varying degrees of wound closure. By day 14, the ChMA–AgNPs group achieved complete re-epithelialization (Fig. S5).

Masson staining showed that the collagen fibers within the ChMA–AgNPs group were denser, and fibroblast activity and organization of deposition were more intense in the proliferation phase (Fig. 6C and D and S6). To evaluate re-epithelialization during wound healing, the length of the newly regenerated epithelium was measured on day 3, 7, and 14 using H&E staining. On day 7, the ChMA–AgNPs sample was better than the control sample, and there was no significant difference between the sample and the blank one, which reached full-coverage on day 14 (Fig. 6D and E and S6).

We performed immunofluorescence staining for inflammatory markers TNF-α and IL-6, vascular marker CD31, and proliferation marker Ki67 on day 3, 7, and 14, respectively (Fig. 6F and G and S7A, B). On day 7, high levels of CD31 were recorded in the ChMA group, ChMA–AgNPs group, and uninfected group, which signify the fact of neovascularization (Fig. 6H). The positive infection group demonstrated a continuous presence of IL-6 and TNF-α by significant overexpression between day 3 and day 14, with the increasing and decreasing trend. On the contrary, other groups had relatively low inflammatory markers (Fig. 6I and J). As the wound healing process progressed, the ChMA–AgNPs group showed a high Ki67 expression on day 3, and then it declined on day 7. In contrast, the positive infection group showed more Ki67 expression than the ChMA–AgNPs group from day 3 to day 7 (Fig. 6K). This, together with the continuing infection, implies impaired and delayed healing in the positive infection group, never having an effective healing microenvironment.

SEM analysis of tissue sections validated the *in vivo* antibacterial properties (Fig. 6L). The control group exhibited abundant bacterial colonization, while the ChMA–AgNPs group showed detectable bacteria on day 3, though at significantly lower levels than the control group. By day 7, no bacterial residues remained detectable in the ChMA–AgNPs group. These results indicate that the ChMA–AgNPs hydrogel effectively blocks invasive infection. Functionally, the chemotaxis-plus-killing strategy resulted in faster epithelial coverage and earlier collagen deposition. The H&E staining of major organs revealed no pathology (Fig. S8).

Collectively, *in vivo* experimental results demonstrate that the composite hydrogel can effectively control CRPA infection, reduce wound inflammatory responses, promote re-epithelialization and collagen deposition, thereby accelerating the healing of infected wounds.

4.6. Investigation of ChMA–AgNPs in wound healing

Global transcriptome differences and early functional responses induced by ChMA-AgNPs Treatment (Fig. 7A–E, Fig. S9 and S10). To systematically evaluate the transcriptomic differences between the ChMA–AgNPs group (A) and the control group (Y) at various post-operative stages, we first performed Principal Component Analysis (PCA). The results demonstrated that the samples clustered distinctly along the PC1 and PC2 axes, revealing the dual driving effects of both the treatment factor and the temporal dimension (day 3 *vs.* day 7) on the gene expression profiles (Fig. 7A). On day 3, functional enrichment analysis of differentially expressed genes (DEGs) showed that up-regulated genes were significantly enriched in pathways such as Ribosome, Wnt signaling, Focal adhesion, and ECM-receptor interaction (Fig. 7B and C and S10A, B). GSEA further revealed the significant activation of inflammatory responses, TNF-α signaling *via* NF-kB, and myeloid cell ageing-related gene sets (Fig. S10C). Concurrently, down-regulated genes were predominantly concentrated in classical inflammatory regulatory pathways, including cytokine–cytokine receptor interaction, chemokine signaling, and MAPK signaling (Fig. S10B).

To resolve more granular dynamic patterns, time-series clustering categorized the DEGs into six core clusters, showcasing the divergent expression trajectories between groups A and Y over time (Fig. 7D). By comparing the enrichment trajectories across the two time points (Pathway Chronology), we observed that development-related pathways, such as Wnt,

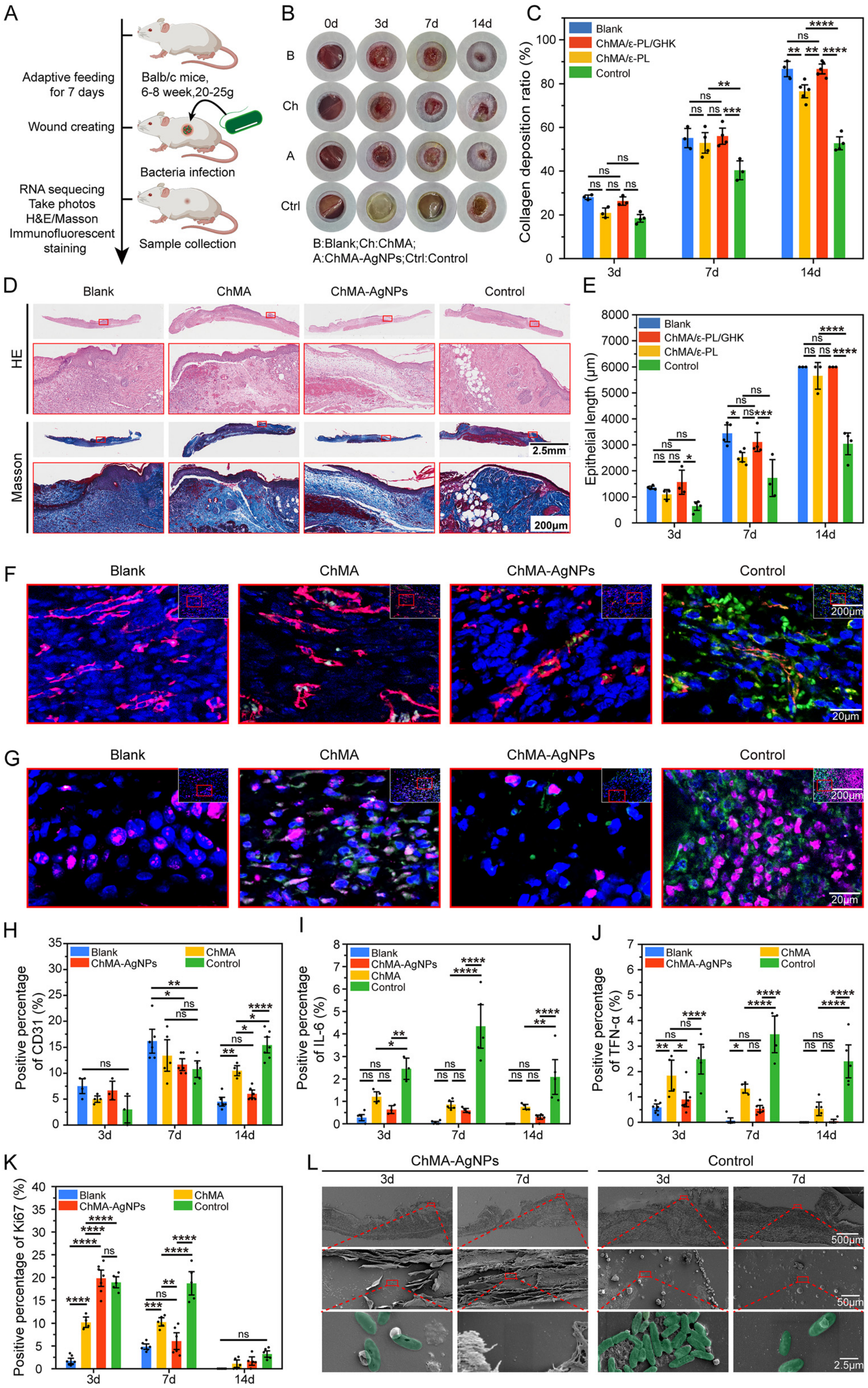

Fig. 6 Evaluation of the *CRPA*-infected wound healing in mice. (A) Schematic of the experiment. (B) Representative images of the wounds. (C) Collagen deposition in the wounds of mice in each group. (D) Representative H&E and Masson staining images of the epithelium on day 7. (E) Statistical analysis of the length of the new epithelium after mouse trauma. (F) Representative images of the CD31 and IL-6 immunofluorescence staining on day 7, with CD31 showing red fluorescence and IL-6 showing green fluorescence. (G) Representative images of the TNF-α and Ki67 immunofluorescence staining on day 7, with Ki67 showing purple fluorescence and TNF-α showing green fluorescence. (H) Relative fluorescence intensity of CD31. (I) Relative fluorescence intensity of IL-6. (J) Relative fluorescence intensity of TNF-α. (K) Relative fluorescence intensity of Ki67. (L) Electron microscopy images of the deep tissue on day 3 and 7 ($n \geq 3$, $P < 0.05$ (*), $P < 0.01$ (**), $P < 0.001$ (***) and ns: nonsignificant difference).

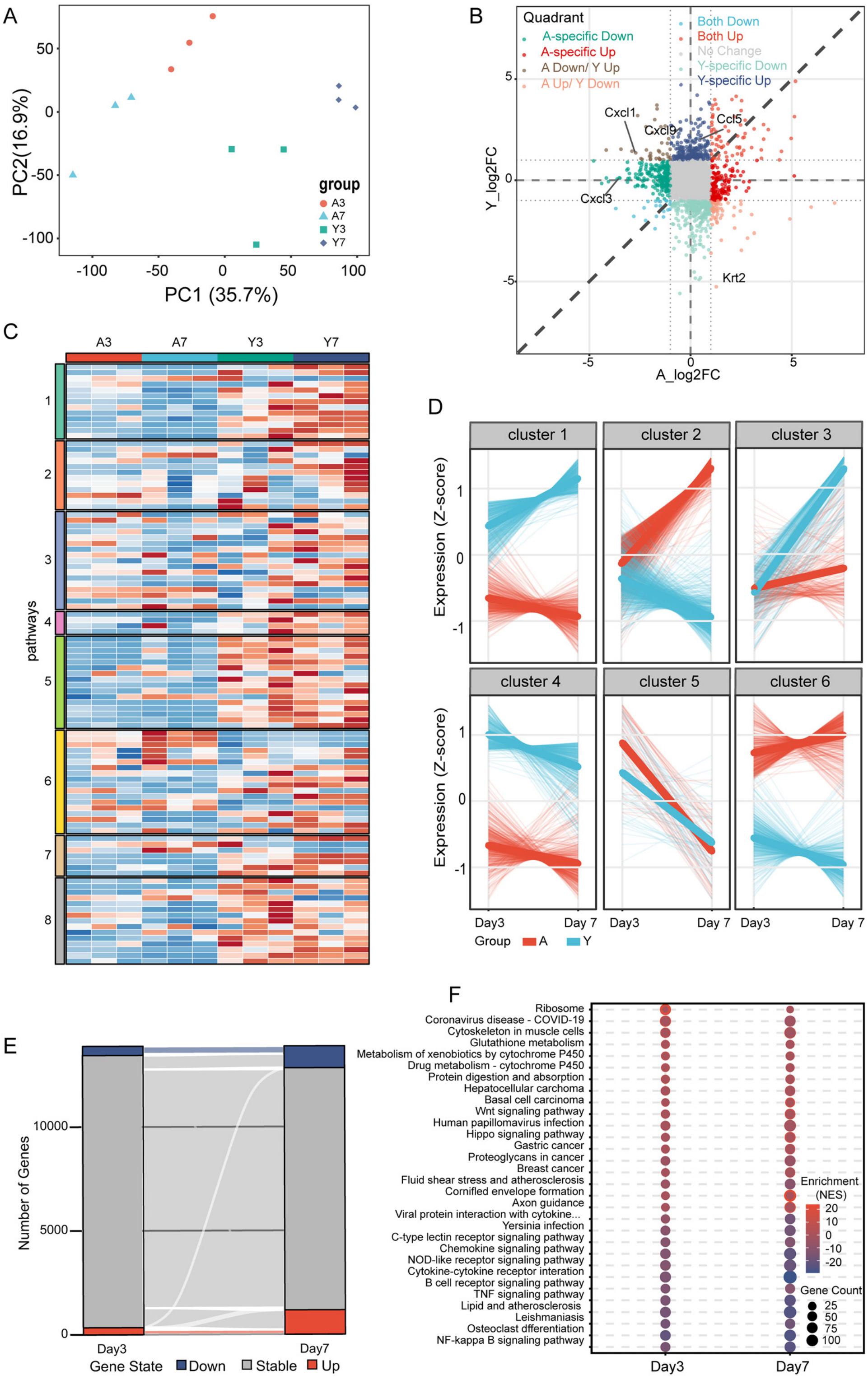

Fig. 7 Global transcriptomic landscape and core functional signatures. (A) Principal component analysis (PCA) of transcriptomic profiles from all groups, highlighting the separation of ChMA–AgNPs (A) and control (Y) groups across timepoints. (B) GSEA dot plot showing significant enrichment of the inflammatory and ageing-related pathways on day 3. (C) KEGG and GO pathways identifying the core-activated biological processes. 1. GO: inflammatory response; 2. GO: antibacterial humoral response; 3. GO: positive regulation of wound healing; 4. GO: antibacterial innate immune response; 5. KEGG: NF-kappa B signaling pathway; 6. KEGG: ECM-receptor interaction; 7. KEGG: neutrophil extracellular trap formation; and 8. KEGG: TNF signaling pathway. (D) Time-series gene expression clustering (clusters 1–6) displaying the dynamic *Z*-score patterns of genes in the A and Y groups. (E) Gene state flow tracking of the differential expression dynamics from day 3 to 7. (F) Pathway chronology dot plot comparing the normalized enrichment scores (NES) of representative pathways between day 3 and 7 ($n \geq 3$, $P < 0.05$ (*), $P < 0.01$ (**), $P < 0.001$ (***) and ns: non-significant difference).

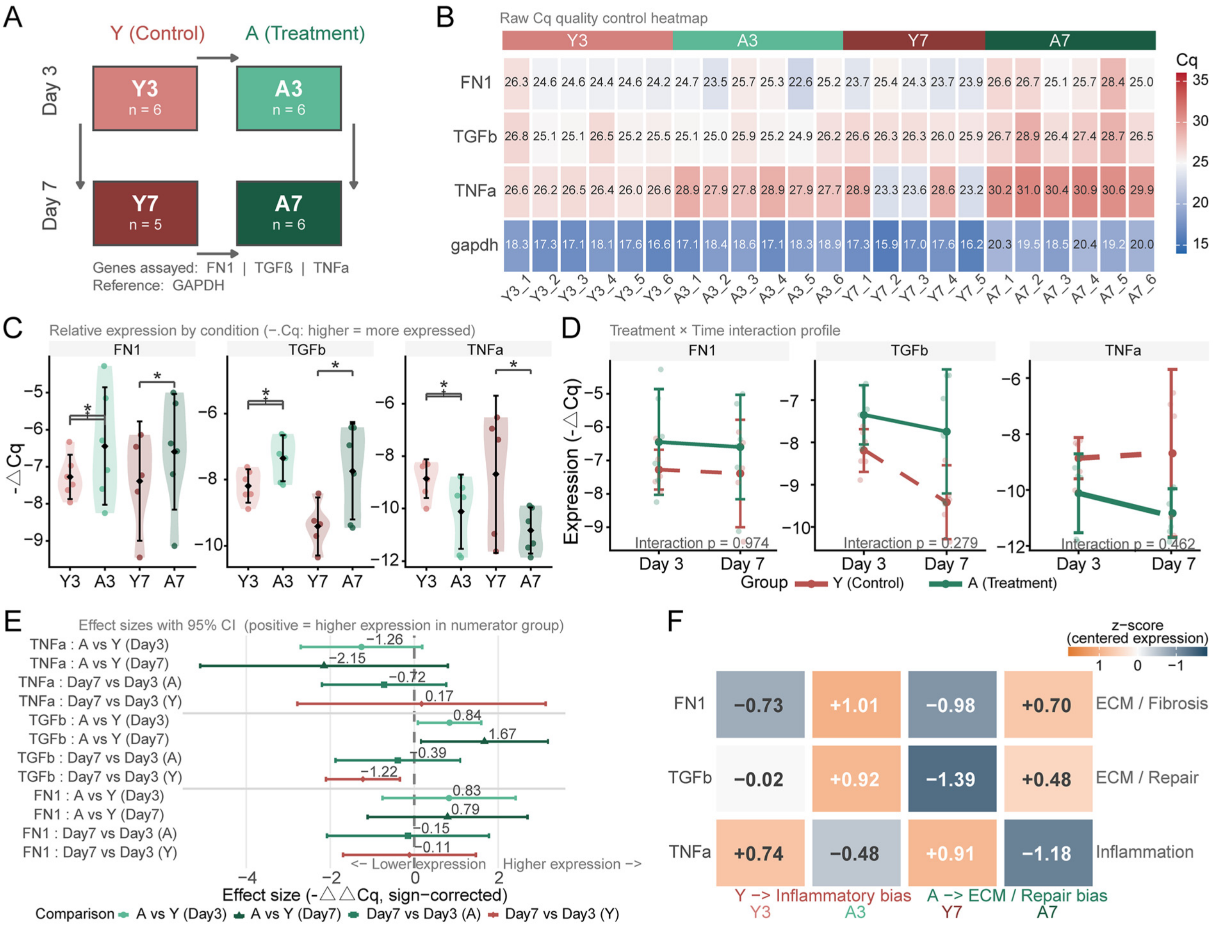

Fig. 8 Functional validation. (A) Schematic of the experimental design. The samples were divided into four groups based on time and treatment: Y3 (control group: day 3, $n = 6$), A3 (ChMA–AgNPs group: day 3, $n = 6$), Y7 (control group: day 7, $n = 5$), and A7 (ChMA–AgNPs group: day 7, $n = 6$). The genes tested were FN1, TGF-β, and TNF-α, with GAPDH as the internal control gene. The red color series represents the Y (control) group, and the green color series represents the A (treatment) group; light and dark colors correspond to days 3 and 7, respectively. (B) Raw Cq quality control heatmap. Each row in the heatmap represents a detected gene (FN1, TGF-β, TNF-α, and GAPDH), and each column represents a replicate of an independent sample. The top color bar indicates different experimental groups: Y3, A3, Y7, and A7. The numbers inside the squares represent the raw Cq values of the corresponding wells. The color scale on the right indicates the magnitude of Cq: blue indicates a lower Cq, suggesting a higher template abundance and red indicates a higher Cq, suggesting a lower template abundance. Red borders indicate the outliers identified based on the IQR method; gray fill indicates Cq > 35; and a dot indicates missing Cq values or a Cq value of 0. This heatmap is used to evaluate the amplification quality, intra-group consistency, and potential abnormal wells of each group of samples. (C) Normalized relative expression distribution plots for each group. The plots show the expression levels of FN1, TGF-β, and TNF-α in groups Y3, A3, Y7, and A7, respectively. The *y*-axis represents $-\Delta$Cq, where a higher value indicates a higher normalized expression level. Each scatter point represents an independent biological replicate; the semi-violin plot represents the intra-group distribution; the black diamond represents the group median, and the black error bar represents the intra-group dispersion. The upper brackets and asterisks indicate the statistical comparison results between groups A and Y at the same timepoint. (D) Treatment × time interaction trend plot. The plot shows the expression change trajectories of FN1, TGF-β, and TNF-α at two time points: days 3 and 7. The *y*-axis represents normalized expression levels ($-\Delta$Cq), and the *x*-axis represents time. The red dashed line represents the Y (control) group, and the green solid line represents the A (treatment) group; dots represent group means, and error bars represent the range of within-group variation. The annotation below the panel indicates the results of the treatment × time interaction test for the corresponding gene, which is used to evaluate whether the effect of treatment A changes over time. (E) Forest plot of effect sizes. The plot displays the effect sizes and their 95% confidence intervals of FN1, TGF-β, and TNF-α in different preset comparisons, including A *vs.* Y (day 3), A *vs.* Y (day 7), day 7 *vs.* day 3 ***(A), and day 7 *vs.* day 3 (Y). The *x*-axis represents the magnitude of the effect size, with positive values indicating higher expression of the former and negative values indicating higher expression of the latter; the dashed line represents the zero-effect reference line. Different colors represent different comparison types used to comprehensively evaluate the direction and intensity of treatment effects and time effects. (F) Comprehensive expression signature heatmap. Each row in the heatmap represents a specific gene (FN1, TGF-β, and TNF-α), and each column represents an experimental group (Y3, A3, Y7, and A7). The values within the grid represent normalized and centered *Z*-scores. The color scale in the upper right corner indicates relative expression levels: orange indicates relatively high expression, and blue indicates relatively low expression. The text on the right side annotates the main biological functional dimensions represented by the corresponding genes, where FN1 mainly corresponds to ECM/fibrosis, TGF-β corresponds to ECM/repair, and TNF-α corresponds to inflammation. The annotation at the bottom summarizes the overall transcriptional bias of each group: Y3 and Y7 are more biased towards inflammatory states, while A3 and A7 are more biased towards ECM/repair-related states ($n \geq 3$, $P < 0.05$ (*), $P < 0.01$ (**), $P < 0.001$ (***) and ns: nonsignificant difference).

Hippo, and Axon guidance, exhibited sustained activation in the treatment group, whereas inflammatory signals were significantly suppressed on both day 3 and day 7 (Fig. 7E and F and S9A, B). Supplementary analysis further indicated that up-regulated pathways on day 7 focused on tissue remodeling, while down-regulated pathways remained consistently associated with NOD-like receptor and TNF signaling (Fig. S11A–C).

We employed qPCR methodology to validate the four groups (Fig. 8A). After normalization with GAPDH, treatment A consistently shifted the transcriptome towards ECM/remodeling-related states on both day 3 and day 7 (Fig. 8C). Specifically, compared to group Y, group A exhibited increased expression of FN1 and TGF-β and decreased expression of TNF-α at both time points (Fig. 8C). Among the three markers, TGF-β showed the most pronounced inter-group separation and the lowest intra-group variability, while FN1 and TNF-α exhibited greater heterogeneity but maintained the same directional trend (Fig. 8C). This pattern was further supported by the treatment × time curve, which demonstrated stable separation between group A and group Y at both time points, with only minor interactive effects (Fig. 8D). Effect size analysis consistently confirmed that FN1 and TGF-β exhibited a positive effect of group A relative to group Y on both day 3 and day 7, while TNF-α exhibited a negative effect (Fig. 8E). At the integrated feature level, centered expression analysis showed that A3 and A7 shifted towards ECM/repair-related states, while Y3 and Y7 remained relatively inflammatory-prone (Fig. 8F). Raw Cq quality control indicated that the detection performance was generally acceptable, but several outliers were detected and the GAPDH values of A7 were overall higher, supporting the use of normalized expression values rather than raw values in downstream interpretation (Fig. 8B). These data collectively suggest that group A promotes repair-related transcriptional programs while inhibiting inflammatory signaling (Fig. 8C–F).

5. Conclusion

This study elucidates the targeted chemotactic mechanism of L-lysine against *CRPA* and develops a ChMA–AgNPs composite hydrogel integrating active chemotaxis, synergistic antibacterial activity, and wound repair functions. Current chemotactic antibacterial strategies mostly rely on passive modes by inhibiting bacterial motility and often suffer from unstable and short-lived chemotactic gradients due to the separation of chemoattractants and antibacterial components.[37,38] In this work, we integrated L-lysine-mediated chemotactic recruitment with silver nanoparticle-based bactericidal functions into a single platform to achieve their synergistic effects. This novelty provides a new treatment modality with respect to *CRPA*-infected wounds. The composite hydrogel which uses ChMA allows the sustained release of L-lysine and stable encapsulation of AgNPs. The material has received high hydrophilicity, mechanical stability, and biocompatibility and effectively reduced the tissue toxicity of silver ions. However, this study still has limitations: the hydrogel has fewer inhibitory activities on *CRPA* biofilms and remains unproven in terms of the targeted eradication of mature biofilms.

Furthermore, the research has only validated its efficacy against specific *CRPA* strains, and its anti-infective effects on other genotypic *Pseudomonas aeruginosa* drug-resistant strains require further investigation. In summary, this hydrogel achieves high-quality repair of *CRPA*-infected wounds through multiple synergistic effects and exhibits great potential for clinical translation. Future formulations could be further optimized by incorporating biofilm inhibitors to enhance the therapeutic efficacy for complex infected wounds.

Author contributions

Xinxin Su and Morui Gui contributed equally to this work. Xinxin Su performed the experiments, curated and analyzed the data, developed the methodology, visualized the results, and wrote the original draft of the manuscript. Morui Gui supervised the experiments, validated the methodology, curated and analyzed the data, and developed the software. Tingna Luo assisted with data curation and formal analysis. Qiqi Liu contributed to formal analysis and experimental investigation. Xiaohong Zhao contributed to the development of biological directional approaches. Yicheng Guo contributed to the research on orientation methodology in materials science. Rixing Zhan designed the flowchart and provided supervision. Zhongshuo Hao assisted in the experimental investigation. Zhongshuo Hao participated in the data analysis. Xinxin Su and Morui Gui drafted the manuscript. Xisheng Xu, Shuncai Liu and Zhenyu Gong conceptualized and guided the research project. All authors proofread the manuscript.

Conflicts of interest

The authors declare no competing financial interests or personal relationships that could influence the work reported in this paper.

Ethics approval and consent to participate

The Ethics Committee of the First Affiliated Hospital of the Army Military Medical University approved the animal testing procedure (AMUWEC20224129).

Data availability

The datasets generated and analysed during the current study are included in this published article and its supplementary information (SI). Supplementary Information includes detailed experimental protocols, raw data from bacterial chemotaxis assays, FTIR spectra, full transcriptomic datasets, original statistical data of *in vitro* antibacterial tests and *in vivo* wound healing experiments, and additional material characterization figures. Supplementary information is available. See DOI: https://doi.org/10.1039/d6bm00417b.

Acknowledgements

The authors would like to express their sincere gratitude to Prof. Rixing Zhan and Prof. Gaoxing Luo for their continuous guidance, support, and inspiration throughout this research. They also thank the Institute of Burn Research at the Southwest Hospital for providing the experimental platforms and technical assistance. This work was supported by the Natural Science Foundation of Guangxi Zhuang Autonomous Region (Grant No. 2024GXNSFAA010170, 2026GXNSFHA00640186), Guangxi Medical and Health Key Research Project (Grant No. S2023103), Guilin Science and Technology Bureau Projects (Grant No. 20220116-1, 20230114-1), National Natural Science Foundation of China (Grant No. 82372514), and Natural Science Foundation of Hunan Province (2025JJ70554).

References

1 J. Wełna, M. Napiórkowska-Mastalerz, M. Cyrankiewicz, T. Bogiel and J. Kwiecińska-Piróg, Characteristic of virulence and parameters of mixed biofilm formed by carbapenem-resistant pseudomonas aeruginosa and proteus mirabilis strains isolated from infected chronic wounds, *Pathogens*, 2025, **14**(6), 536–553.

2 I. C. Cunha-Ferreira, C. S. Vizzotto, J. Peixoto and R. H. Krüger, Antibiotic resistance crisis: From bacterial bioprospecting to artificial intelligence, *Environ. Microbiol. Rep.*, 2025, **17**(6), e70267.

3 L. Xiao, Y. Guo, F. Wang, *et al.*, A 3D chemotactic-thermo-promo bacterial hunting system: Programmatic bacterial attract, capture, killing and healing the wound, *Chem. Eng. J.*, 2021, **417**, 128123.

4 Z. Li, X. Xing, C. Zhao, *et al.*, A rapid interactive chitosan-based medium with antioxidant and pro-vascularization properties for infected burn wound healing, *Carbohydr. Polym.*, 2024, **333**, 121991.

5 M. Kumar, D. Kumar, Y. Garg, S. Mahmood, S. Chopra and A. Bhatia, Marine-derived polysaccharides and their therapeutic potential in wound healing application - a review, *Int. J. Biol. Macromol.*, 2023, **253**, 127331.

6 X. Li, S. Sun, A. Yang, *et al.*, Dual-crosslinked methacrylamide chitosan/poly(ε-caprolactone) nanofibers sequential releasing of tannic acid and curcumin drugs for accelerating wound healing, *Int. J. Biol. Macromol.*, 2023, **253**, 127601.

7 H. O. Khalifa, A. Oreiby, T. Mohammed, *et al.*, Silver nanoparticles as next-generation antimicrobial agents: Mechanisms, challenges, and innovations against multi-drug-resistant bacteria, *Front. Cell. Infect. Microbiol.*, 2025, **15**, 1599113.

8 A. Sousa, A. T. Rufino, R. Fernandes, *et al.*, Silver nanoparticles exert toxic effects in human monocytes and macrophages associated with the disruption of δψm and release of pro-inflammatory cytokines, *Arch. Toxicol.*, 2023, **97**(2), 405–420.

9 P. Yang, Y. Hu, Y. Ju, *et al.*, DNA-inspired multi-functional double-cross-linking self-healing hydrogel promotes the healing of diabetic wounds, *Adv. Sci.*, 2026, **13**(8), e13784.

10 H. Xue, C. Zhang, D. Lin, *et al.*, Isoliquiritigenin micellar microneedle for pH monitoring and diabetic wound healing, *Mater. Today. Bio*, 2025, **35**, 102356.

11 A. Jin, H. Xue, Z. Jia, *et al.*, NIR/pH-responsive multifunctional hydrogel for monitoring and treating diabetic wounds, *Adv. Healthcare Mater.*, 2026, e05403.

12 Y. Li, R. Liang, Y. Ju, *et al.*, Magnesium-EGCG composite deer antler decellularized ECM hydrogel for diabetic wound healing, *Nano Res.*, 2026, **19**(1), 94908255.

13 U. Bozuyuk, O. Yasa, I. C. Yasa, H. Ceylan, S. Kizilel and M. Sitti, Light-Triggered Drug Release from 3D-Printed Magnetic Chitosan Microswimmers, *ACS Nano*, 2018, **12**(9), 9617–9625.

14 X. Li, S. Sun, A. Yang, *et al.*, Dual-crosslinked methacrylamide chitosan/poly(ε-caprolactone) nanofibers sequential releasing of tannic acid and curcumin drugs for accelerating wound healing, *Int. J. Biol. Macromol.*, 2023, **253**, 127601.

15 X. Yu, D. He, X. Zhang, *et al.*, Surface-adaptive and initiator-loaded graphene as a light-induced generator with free radicals for drug-resistant bacteria eradication, *ACS Appl. Mater. Interfaces*, 2019, **11**(2), 1766–1781.

16 Z. Liao, X. Su, T. Luo, *et al.*, A side-effect-free chemotactic-antibacterial wound dressing for programmatic trapping, killing of bacteria, and wound repair, *Mater. Today. Bio*, 2025, **35**, 102594.

17 J. Cremer, T. Honda, Y. Tang, J. Wong-Ng, M. Vergassola and T. Hwa, Chemotaxis as a navigation strategy to boost range expansion, *Nature*, 2019, **575**(7784), 658–663.

18 R. Jain, N. G. Faith, A. Milkowski, *et al.*, Using chemoattractants to lure bacteria to contact-killing surfaces, *Angew. Chem.*, 2016, **128**(19), 5792–5796.

19 N. M. Oliveira, J. H. R. Wheeler, C. Deroy, *et al.*, Suicidal chemotaxis in bacteria, *Nat. Commun.*, 2022, **13**(1), 7608.

20 J. R. Seymour, D. R. Brumley, R. Stocker and J.-B. Raina, Swimming towards each other: The role of chemotaxis in bacterial interactions, *Trends Microbiol.*, 2024, **32**(7), 640–649.

21 A. M. Kollaran, S. Joge, H. S. Kotian, *et al.*, Context-specific requirement of forty-four two-component loci in pseudomonas aeruginosa swarming, *iScience*, 2019, **13**, 305–317.

22 A. E. Mattingly, N. G. Kamatkar, N. Morales-Soto, B. R. Borlee and J. D. Shrout, Multiple environmental factors influence the importance of the phosphodiesterase DipA upon pseudomonas aeruginosa swarming, *Appl. Environ. Microbiol.*, 2018, **84**(7), e02847–e02817.

23 A. Waghmare and Y. Bhargava, Tunable effect of divalent cations on tendril patterning during swarming motility of pseudomonas aeruginosa, *Chem. Eng. J.*, 2025, **509**, 161465.

24 N. A. Negm, H. H. H. Hefni, A. A. A. Abd-Elaal and E. A. Badr, Abou Kana MTH. Advancement on modification of chitosan biopolymer and its potential applications, *Int. J. Biol. Macromol.*, 2020, **152**, 681–702.

25 F. Zhou, C. Cui, S. Sun, *et al.*, Electrospun ZnO-loaded chitosan/PCL bilayer membranes with spatially designed structure for accelerated wound healing, *Carbohydr. Polym.*, 2022, **282**, 119131.

26 A. Moeini, P. Pedram, P. Makvandi, M. Malinconico and G. Gómez d'Ayala, Wound healing and antimicrobial effect of active secondary metabolites in chitosan-based wound dressings: A review, *Carbohydr. Polym.*, 2020, **233**, 115839.

27 C. Van Poucke, E. Verdegem, S. Mangelinckx and C. V. Stevens, Synthesis and unambiguous NMR characterization of linear and branched N-alkyl chitosan derivatives, *Carbohydr. Polym.*, 2024, **337**, 122131.

28 M. Zanon, A. Chiappone, N. Garino, *et al.*, Microwave-assisted methacrylation of chitosan for 3D printable hydrogels in tissue engineering, *Mater. Adv.*, 2022, **3**(1), 514–525.

29 Y. Xu, Z. Deng, Y. Chen, F. F. Wu, C. Huang and Y. Hu, Preparation and characterization of mussel-inspired hydrogels based on methacrylated catechol-chitosan and dopamine methacrylamide, *Int. J. Biol. Macromol.*, 2023, **229**, 443–451.

30 W. Feng, M. Chittò, W. Xie, *et al.*, Poly(D-amino acid) Nanoparticles Target *Staphylococcal* Growth and Biofilm Disassembly by Interfering with Peptidoglycan Synthesis, *ACS Nano*, 2024, **18**(11), 8017–8028.

31 S. Zhang, W. He, J. Dong, Y. K. Chan, S. Lai and Y. Deng, Tailoring Versatile Nanoheterojunction-Incorporated Hydrogel Dressing for Wound Bacterial Biofilm Infection Theranostics, *ACS Nano*, 2025, **19**(11), 10922–10942.

32 Y. Zhan, X. Hu, Y. Li, *et al.*, Antimicrobial Hybrid Amphiphile via Dynamic Covalent Bonds Enables Bacterial Biofilm Dispersal and Bacteria Eradication, *Adv. Funct. Mater.*, 2023, **33**(23), 2214299.

33 J. Wu, F. Li, X. Hu, *et al.*, Responsive Assembly of Silver Nanoclusters with a Biofilm Locally Amplified Bactericidal Effect to Enhance Treatments against Multi-Drug-Resistant Bacterial Infections, *ACS Cent. Sci.*, 2019, **5**(8), 1366–1376.

34 K. E. Cherny and K. Sauer, Pseudomonas aeruginosa requires the DNA-specific endonuclease EndA to degrade extracellular genomic DNA to disperse from the biofilm, *J. Bacteriol.*, 2019, **201**(18), e00059-19.

35 P. Rao, J. B. Aswathanarayan, S. V. Madhunapantula, R. V. Rai, P. Ramasami and S. G. Shivappa, Enhanced biofilm disruption in ESKAPE pathogens through synergistic activity of EPS degrading enzymes, *Pure Appl. Chem.*, 2025, **97**(5), 503–516.

36 S. N. Vahdati, H. Behboudi, S. A. Navasatli, S. Tavakoli and M. Safavi, New insights into the inhibitory roles and mechanisms of D-amino acids in bacterial biofilms in medicine, industry, and agriculture, *Microbiol. Res.*, 2022, **263**, 127107.

37 R. Jain, N. G. Faith, A. Milkowski, *et al.*, Using chemoattractants to lure bacteria to contact-killing surfaces, *Angew. Chem.*, 2016, **128**(19), 5792–5796.

38 M. A. Matilla and T. Krell, Targeting motility and chemotaxis as a strategy to combat bacterial pathogens, *Microb. Biotechnol.*, 2023, **16**(12), 2205–2211.